Active site manipulation in MoS_2 cluster electrocatalysts by transition metal doping

Jo J. L. Humphrey[1], Rasmus Kronberg[2], Rongsheng Cai,[3] Kari Laasonen[2], Richard E. Palmer,[3] Andrew J. Wain[*1]

[1]National Physical Laboratory, Hampton Road, Teddington, TW11 0LW, United Kingdom
[2]Department of Chemistry and Materials Science, Aalto University, P.O. Box 16100, 00076 Aalto, Finland
[3]College of Engineering, Swansea University, Bay Campus, Fabian Way, Swansea, SA1 8EN, United Kingdom

[*]Corresponding author: andy.wain@npl.co.uk

Abstract

The development of non-platinum group metal catalysts for the hydrogen evolution reaction (HER) in water electrolyser devices is essential for their widespread and sustainable deployment. In recent years, molybdenum disulfide (MoS_2) catalysts have received significant attention as they not only exhibit good electrocatalytic HER activity but also, crucially, acid-stability. However, further performance enhancement is required for these materials to be competitive with Pt and to that end transition metal doping of MoS_2 has been explored as a route to further increasing its catalytic activity. In this work, cluster beam deposition was employed to produce controlled cobalt-doped MoS_2 clusters (MoS_2-Co). We demonstrate that, in contrast to previous observations of performance enhancement in MoS_2 resulting from nickel doping (MoS_2-Ni), the introduction of Co has a detrimental effect on HER activity. The contrasting behaviours of Ni and Co doping are rationalized by density functional theory (DFT) calculations, which suggest that HER-active surface vacancies are deactivated by combination with Co dopant atoms, whilst their activity is retained, or even partially enhanced, by combination with Ni dopant atoms. Furthermore, the adatom dopant-vacancy combination kinetics appear to be more than three orders of magnitude faster in MoS_2-Co than for MoS_2-Ni. These findings highlight a fundamental difference in the influence of transition metal dopants on the HER performance of MoS_2 electrocatalysts and stress the importance of considering surface atomic defects when predicting their behaviour.

Keywords

Molybdenum disulfide; hydrogen evolution; cluster beam deposition; doping; DFT

1. Introduction

Water electrolysers are expected to play a major role in the future energy landscape, offering a clean approach to storing renewable energy in the form of hydrogen fuel. However, at present these devices rely on rare and expensive platinum group metals as electrocatalysts to split water efficiently, which limits their widespread implementation. Hence, there is a need to develop alternative earth-abundant electrocatalysts with high activity and stability.

Over the last decade, molybdenum disulfide (MoS_2) has emerged as a promising alternative catalyst for the hydrogen evolution reaction (HER),[1-4] but its chemical synthesis suffers drawbacks such as the need for high temperatures[3] and limited control over catalyst structure and composition. Numerous chemical routes have been explored in an attempt to tune the structure of MoS_2 catalyst materials, predominantly with a view to exposing the highly active edge sites.[1, 4, 5] For example, Kibsgaard *et al*. prepared an edge-rich, mesoporous double gyroid continuous MoS_2 film by depositing Mo into a silica template and subsequent sulfurization.[4] Other examples include the preparation of MoS_2 nanoflowers by hydrothermal synthesis,[6] MoS_2 nanodots by ionic liquid-assisted exfoliation,[7] and MoS_2 nanocone arrays by plasma etching,[8] in order to increase the active edge density. Whilst these materials advances are promising, there is still significant room for improvement in performance in order to compete with the state-of-the-art catalyst, Pt. An alternative approach to structural optimization in MoS_2 is to introduce dopant heteroatoms such as transition metals (TMs) in order to modify the electronic structure in an attempt to improve catalytic activity.[9-11] However, such approaches are exceptionally complex, as they are highly dependent on both the synthetic technique, dopant level, and location of dopant atoms.

Experimental catalyst development can be enhanced and complemented by first-principles electronic structure calculations based on, for example, density functional theory (DFT). Recent DFT calculations on electrochemical systems have indeed produced highly encouraging results, providing refined insight into fundamental structure-activity relationships of HER electrocatalysts among others.[12, 13] Previous computational studies[14] on transition metal (Fe, Co, Ni, Cu) doping of the 2H-MoS_2 basal plane suggest clear benefits; H-adsorption in the vicinity of dopant atoms is optimally strengthened compared to the pristine basal plane, which exhibits a negligible hydrogen affinity. On the other hand, doping of the undercoordinated Mo- and S-edges results in complex long-range modifications of both the atomic and electronic structure which may be either preferential or deleterious with respect to the HER activity. In particular, pristine MoS_2 edges exhibiting preferential hydrogen adsorption properties are generally seen to deactivate upon TM-doping, while initially inert edge-sites are activated. However, previous calculations do not indicate a clear correlation between specific dopant atoms and the hydrogen affinity of adjacent sites, *i.e.* a given dopant atom is observed to improve as well as worsen the hydrogen affinity depending on the considered edge type.

In addition to TM-doping, activation of the MoS_2 basal plane for HER catalysis can be achieved by introducing defects. Defect-sites, particularly various sulfur vacancies, are suggested by DFT calculations to exhibit remarkably improved hydrogen adsorption properties.[15, 16] This conclusion is well-supported by experimental studies, demonstrating the synergistic effects of combining theoretical simulations with experiments.[17] However, it is noteworthy that previous studies have largely neglected the interplay between dopant atoms and defect sites in MoS_2. Thus, a comprehensive atomistic picture of realistic TM-doped and defect-containing MoS_2 is still lacking.

In order to thoroughly investigate such effects experimentally, controlled synthesis of MoS_2, and the ability to tune dopant levels, are critical. Cluster beam deposition (CBD) is one such method which offers a physical route to obtaining cluster catalysts with notable control over cluster size, composition and morphology.[18, 19] Compared with traditional chemical methods, no solvents, salts or ligands are needed during the synthesis process,[20, 21] making it an environmentally-friendly and in principle sustainable method. Since metal atoms are simply mixed together in the vacuum chamber to form clusters, it is relatively easy to develop recipes for new cluster systems. Recently, this approach has been used for controlled doping of MoS_2 clusters with Ni.[11] The electrochemical HER performance of Ni-doped MoS_2 clusters was compared to that of the pure MoS_2 and Ni cluster materials in perchlorate electrolyte at pH 3. The results indicated that Ni doping does indeed improve the catalytic HER activity of the MoS_2 clusters, with the Ni-MoS_2 material demonstrating a 100 mV reduction in the HER onset potential, which was attributed to an increase in the activity of S edge sites upon inclusion of Ni, which is further improved by its oxidation to Ni^{2+}.[11] It is worth noting, however, that doping effects on the basal plane could not be ruled out.

In this work, the addition of Co to MoS_2 clusters prepared by CBD was explored, specifically to investigate the effect of Co dopants on the electrocatalytic HER activity. The performance of the clusters was assessed in perchlorate electrolyte solution and compared to previous work on analogously prepared Ni-doped MoS_2 clusters.[11] In order to explain the observed differences in the influence of these neighbouring TM dopants on the HER activity of MoS_2 clusters, DFT calculations were performed with particular emphasis on previously omitted dopant-vacancy interactions and their effects on hydrogen adsorption properties.

2. Experimental

2.1. Cluster deposition

Cluster-modified electrodes were produced using a dual-target magnetron sputtering, gas condensation cluster beam source (located at Teer Coatings, Droitwich, UK), detailed information about which has been described in earlier reports.[21, 22] MoS_2, Co and MoS_2-Co binary clusters were deposited onto 5 mm diameter glassy carbon (GC) disk electrodes, which were pre-polished with alumina slurry (0.05 μm) on microfiber cloths and rinsed fully by 3 rounds of sonication in ultrapure water (Elga, 18.2 MΩ cm) prior to cluster deposition.

In the source chamber, two magnetrons (MoS_2 and Co) were mounted in parallel with a condensation length (from the targets to the exit nozzle of the condensation chamber) of approximately 25 cm. The sputtering power applied to each magnetron was controlled separately. By changing the power ratio applied to the MoS_2 and Co magnetrons, the chemical composition of the resulting binary MoS_2-Co clusters was varied from MoS_2-rich to Co-rich. In the preparation of pure MoS_2 and pure Co clusters, only the magnetron with the relevant target was in operation. Detailed parameters used for the cluster deposition are summarized in Table S1 in the Supporting Information. The sputtered atoms were condensed in cold Ar/He gas to form clusters of various sizes and the positively charged portion was deposited onto GC electrodes mounted on a manipulator which can scan along both *x* and *y* directions automatically to achieve a homogeneous cluster coverage. The GC electrodes were biased to a potential of -900 V during the deposition to immobilize the cationic clusters onto the electrode surface. A lateral time of flight mass filter was also used to monitor the cluster mass distribution in the gas phase.

2.2. Cluster Characterization

The cluster size and atomic structure were characterized by a Thermo Fisher Titan Scanning Transmission Electron Microscope (STEM) equipped with a spherical aberration probe corrector (CEOS) and ChemiSTEM Super-X Energy Dispersive X-ray Spectroscopy (EDS) detector at a convergence angle of 21 mrad and a high angle annular dark field (HAADF) detector operating with an inner angle of 55 mrad at 200 kV. EDS mapping in STEM mode was employed to characterise the elemental distribution of individual clusters. STEM samples were prepared by directly depositing clusters onto copper grids coated with an amorphous carbon film in parallel with the deposition of the electrode samples. As the samples were deposited in parallel, the STEM images reflect the cluster density and size distribution of the catalysts used for electrochemical performance testing.

2.3. Electrochemical HER Performance

Glassware was cleaned by soaking overnight in concentrated HNO_3 (70%) and then rinsing three times with ultrapure water (18.2 MΩ cm, Elga). Between uses, the glassware was soaked in concentrated H_2SO_4 and rinsed a further three times with ultrapure water prior to experiments. A solution 0.1 M $NaClO_4$ + 2 mM $HClO_4$ (pH 2.8) was prepared using ultrapure water. This solution was chosen as the electrolyte due to the non-coordinating nature of the perchlorate ion, and to allow for direct comparison with previous work on Ni-doped MoS_2 clusters.[11]

Electrochemical experiments were carried out using an Ivium CompactStat potentiostat. A three-electrode configuration was used, which included the GC working electrode, a saturated mercury/mercurous sulfate (MSE) reference electrode and a GC rod as the counter electrode. Potentials were converted to the normal hydrogen electrode (NHE) scale after experiments (NHE = MSE + 0.69 V), and all potentials herein are quoted *versus* this reference potential unless otherwise stated.

The electrolyte was deaerated by vigorous purging with nitrogen before and during measurements. The catalyst was initially activated by performing 10 potential cycles between +0.2 V and -1.3 V at 50 mV/s. Linear sweep voltammograms (LSVs) were recorded from 0.0 V to -1.2 V at several scan rates between 1200 mV/s and 2 mV/s.

2.4. Density Functional Theory Calculations

All DFT calculations were performed with the CP2K/Quickstep quantum chemistry code.[23, 24] The spin-polarized formulation of the hybrid Gaussian and plane wave (GPW) method[25] was used with an auxiliary plane wave basis cut-off of 550 Ry and a 60 Ry relative cut-off value. In each calculation the generalized gradient approximation (GGA) was invoked by applying the exchange-correlation functional of Perdew, Burke and Ernzerhof (PBE)[26] together with semi-empirical dispersion interaction corrections according to the DFT-D3 scheme of Grimme *et al.*[27, 28] The Becke-Johnson damping function was employed.[29]

The 1s, $3s^2p^4$, $4s^2p^6d^55s^1$, $3s^2p^6d^74s^2$ and $3s^2p^6d^84s^2$ electrons of H, S, Mo, Co and Ni were treated as valence states, respectively, and the corresponding Kohn-Sham orbitals were expanded in molecularly optimized double-ζ plus polarization quality Gaussian basis sets (MOLOPT-SR-DZVP).[30] The remaining ionic cores were represented by norm-conserving scalar relativistic Goedecker-Teter-Hutter (GTH) pseudopotentials.[31-33] The orbital transformation (OT) method[34] using direct inversion in the iterative subspace (DIIS) was employed for iteratively solving the Kohn-Sham equations. The energy convergence criterion for the self-consistent field (SCF) loop was defined as 2.7×10^{-5} eV. The atomic structures were relaxed in the geometry optimization calculations by using the BFGS algorithm until

the force on any atom was less than 2.3×10^{-2} eV/Å. Minimum energy paths were optimized by applying the climbing image nudged elastic band (CI-NEB) method[35] with an 8.0×10^{-2} eV/Å convergence criterion for the maximum force. The Hessian for the normal mode analysis of adsorbed intermediates to estimate adsorption free energies was constructed using finite displacements of $\pm 5.3 \times 10^{-3}$ Å of the involved atoms along the three Cartesian coordinates.

A (6 × 6) bilayer model of the MoS_2 basal plane was employed in all calculations, consisting of 36 MoS_2-units per layer. Computationally optimized lattice constants of a = 3.14 Å and c = 12.12 Å for the pristine bilayer were used. From this pristine bilayer configuration, a single sulfur atom was removed to create a sulfur vacancy (V_S) and either a Co- or Ni-dopant was introduced in a substitutional (replacing Mo) or adatom position, yielding vacancy and dopant surface concentrations of roughly 1.4 at%, respectively. The employed supercell dimensions were $18.8 \times 16.3 \times 36.4$ Å^3 in all calculations and spurious interactions between periodic copies of the system were removed by applying the method of Martyna and Tuckerman.[36] Explicit solvation effects were excluded from the performed DFT calculations, as the presence of a water bilayer has been shown to have a relatively insignificant effect on hydrogen chemisorption energies.[37] This is a consequence of the weak interaction of hydrogen adatoms with the aqueous contact layer.

3. Results and Discussion

3.1. STEM Characterizations of Cluster Catalysts

MoS_2 clusters doped with two different amounts of Co, as well as pure MoS_2 and pure Co clusters, were deposited onto GC electrodes by changing the power applied to the MoS_2 and Co magnetrons. Figure 1 shows the cluster mass spectra in the gas phase corresponding to the four cluster decorated samples. The pure MoS_2 cluster sample (10 W applied to the magnetron) has the smallest peak at ~8.2×10^4 amu, which is equivalent to $(MoS_2)_{500}$ (a cluster containing 500 MoS_2 units). After adding a small amount of Co (5 W applied to the magnetron), the cluster peak shifted to ~2.5×10^5 amu, equivalent to $(MoS_2)_{1500}$, which indicates that adding Co can promote atom aggregation during the cluster formation. This is further confirmed by increasing the sputtering power on the Co magnetron to 35 W causing a cluster peak at ~4.0×10^5 amu ($(MoS_2)_{2500}$). The pure Co cluster sample has two separated peaks located at $(MoS_2)_{2500}$ and $(MoS_2)_{4000}$. These four samples are denoted as MoS_2, MoS_2-Co(-), MoS_2-Co(+) and Co, respectively, in the discussion below, in which the (-) and (+) refer to low and high Co doping levels, respectively.

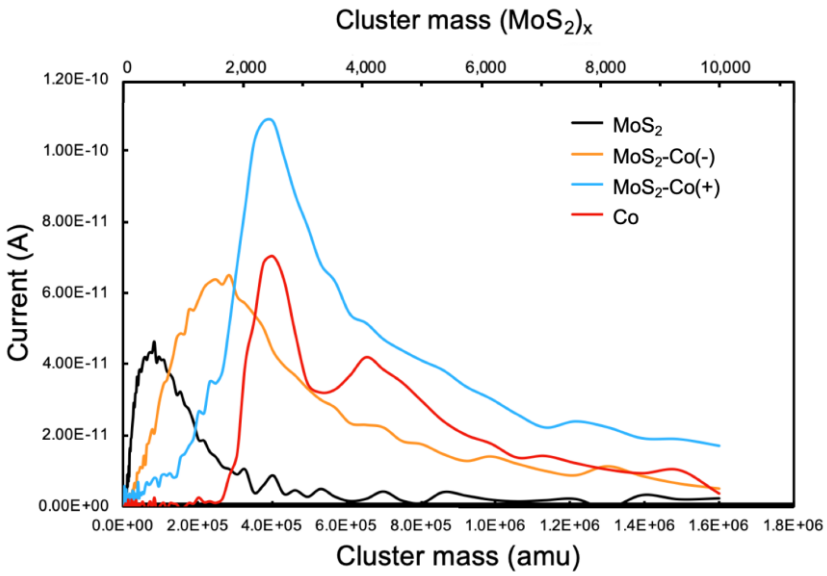

Figure 1. Cluster mass spectra corresponding to the preparation of cluster-decorated electrodes. The cluster peaks are located at ~8.2 × 10^4 amu, ~2.5 × 10^5 amu and ~4.0 × 10^5 amu for MoS_2, MoS_2-Co(-) and MoS_2-Co(+) samples, respectively; the Co cluster sample has two separate peaks at ~4.0 × 10^5 amu and ~6.5 × 10^5 amu.

To reveal the cluster size distribution and atomic structure, HAADF-STEM images were obtained from the samples deposited on TEM grids. Figure 2 shows the HAADF-STEM images from low magnification (top panels) to high magnification (middle panels) and their corresponding size distribution histograms (bottom panels) for each sample. As can be seen from the low magnification images, clusters are well-dispersed on the surface with a similar projected area coverage (between 8% and 11%) in all cases. However, it is clear from the high magnification images that the four cluster samples exhibit different atomic structures and morphologies. The pure MoS_2 clusters have an amorphous structure with open, composite appearance, which can also be described as an incomplete multilayer structure, as observed in our previous study.[11] When MoS_2 clusters were doped with a small amount of Co, the resulting MoS_2-Co(-) clusters retain a similar amorphous structure but become more compact, indicating that the Co is mixed with MoS_2. However, when doped with a large amount of Co, the resulting MoS_2-Co(+) clusters exhibit a phase segregation by forming a core-shell structure with a compact structure (crystalline) in the core and an open structure (amorphous) in the shell as found for pure MoS_2 and MoS_2-Co(-) clusters. This structure is believed to be the first report in the MoS_2 hybrid system at such scale. For the Co cluster sample, most of the clusters possess a quasi-spherical shape with a well-defined face centred cubic (fcc) structure. The bottom panels in Figure 2 show the cluster diameter distribution with peaks at 5.35 nm, 9.26 nm, 6.99 nm and 5.27 nm for MoS_2, MoS_2-Co(-), MoS_2-Co(+) and Co clusters, respectively. From MoS_2 to MoS_2-Co(-), since the cluster structure did not change dramatically, the cluster diameter trend agrees with the mass spectra, with the size becoming larger and wider. However, from MoS_2-Co(-) to MoS_2-Co(+), the peak diameter narrows and does not

match the trend observed from the mass spectra due to the formation of a compact structure in the core of the MoS_2-Co(+) clusters.

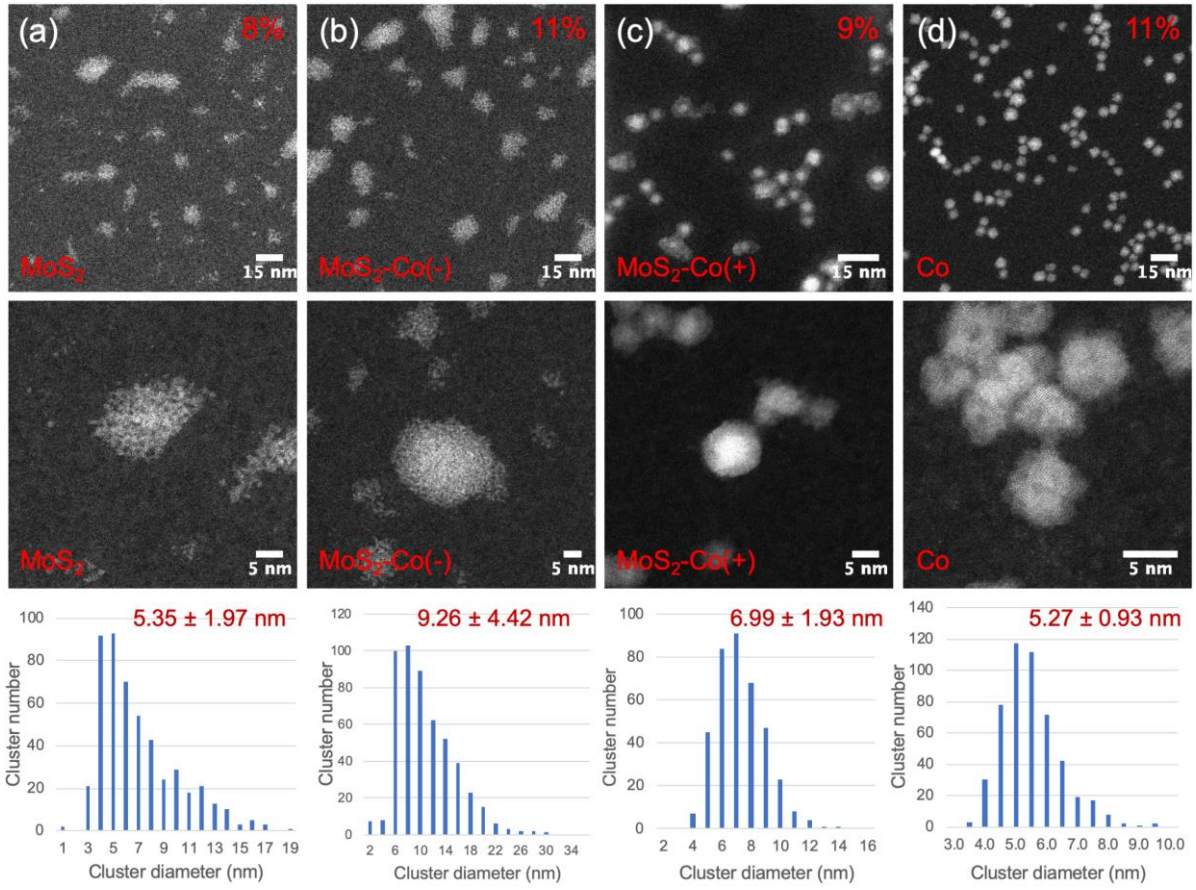

Figure 2. Typical low magnification (top panels) and high magnification (middle panels) HAADF STEM images and their corresponding size distribution histograms (bottom panels) of (a) MoS_2, (b) MoS_2-Co(-), (c) MoS_2-Co(+) and (d) Co clusters. The inset percentage values indicate the measured cluster surface coverages.

To explore the spatial arrangement of the atoms in individual hybrid MoS_2/Co clusters, EDS elemental mapping was conducted on MoS_2-Co(-) and MoS_2-Co(+) clusters, as shown in Figure 3. It can be seen that Co, Mo and S signals were all observed for the MoS_2-Co(-) cluster, and were well-mixed, indicating that Co is completely and homogeneously dispersed throughout the whole MoS_2 cluster in the form of single atoms or clusters below 1 nm in size (based on the spatial resolution of the STEM measurement). Meanwhile, for the MoS_2-Co(+) sample, the shell and core were separately dominated by MoS_2 and Co, respectively, suggesting the formation of a Co-rich/MoS_2-rich core/shell structure in MoS_2-Co(+) sample. It should be noted that the chemical compositions for every cluster are not the same, which was similarly observed in Ni-doped MoS_2 clusters.[11] Based on the EDS mapping results, Co ratios for several individual hybrid MoS_2/Co clusters were analysed by integrating total Co, S and Mo signals, and summarized in Table S2. From this it can be estimated that the average Co content of the MoS_2-Co(-) sample is of the order of a few atomic percent, whilst that of MoS_2-Co(+), is notably higher, at

nearly 80% Co. Whilst more statistical data and elemental analysis would be required to gain an accurate assessment of the Co doping level, it is reasonable to conclude that the two hybrid Co/MoS_2 samples represent the two extremes of Co content.

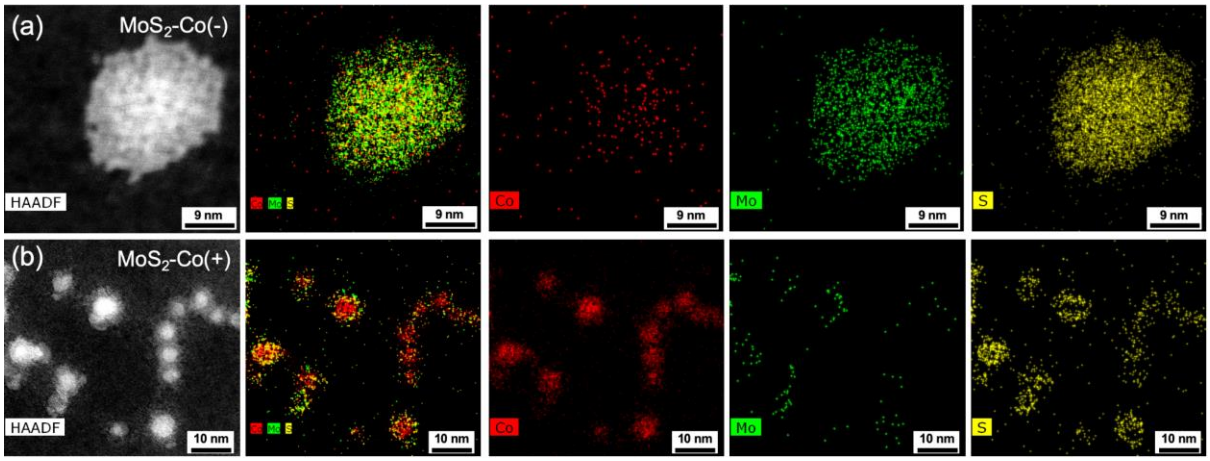

Figure 3. Elemental distribution analysis of two Co-doped MoS_2 cluster samples recorded by aberration-corrected STEM and EDS. (a) Typical HAADF image and corresponding elemental distributions of Co (red), Mo (green) and S (yellow), for MoS_2-Co(-) clusters (b) Typical HAADF image and corresponding elemental distributions for MoS_2-Co(+) clusters.

Based on the cluster size distribution and elemental composition established above, along with the known total mass of clusters deposited, it is possible to estimate the total cluster surface area in each sample (Table 1 and S3). The calculations suggest an increase in total surface area with increasing Co-content, by up to a factor of four, which should be considered when analysing the electrochemical performance data.

3.2. Electrochemical Characterization

Figure 4a shows LSVs of the various cluster catalysts, alongside that of the bare glassy carbon substrate for comparison. Electrochemical preconditioning experiments undertaken prior to recording these LSVs indicated that the samples were relatively stable with electrochemical testing, as shown in Figure S1a. In all cases the current density in Figure 4a has been calculated by normalizing to the geometric area (0.2 cm^2) of the sample. For all cluster samples, a well-defined cathodic wave is observed which is attributed to the HER. The voltammetry exhibits a peak shape, reflecting the local depletion of protons occurring at more negative potentials due to the relatively low proton concentration in the electrolyte solution (~ 2×10^{-6} mol cm^{-3}). Although such experimental conditions are atypical compared to conventional HER electrocatalyst performance testing, they were deliberately used in earlier published work on Ni-doped clusters in order to facilitate kinetic analysis and surface area coverage calculations based on the irreversible Randles-Ševčík equation.[11] Whilst the latter was not attempted in the present

work, it was necessary to perform measurements under identical conditions to make a meaningful comparison between the Ni and Co dopant effects.

The peak current was found to show a linear dependence on the square root of scan rate, confirming that the process is under diffusional control (Figure S1b, c). It is noteworthy that all of the cluster catalyst samples exhibit comparable peak currents, indicating they are operating under similar diffusional regimes. This simplifies comparison between samples and allows the peak potential to be used as a figure of merit.

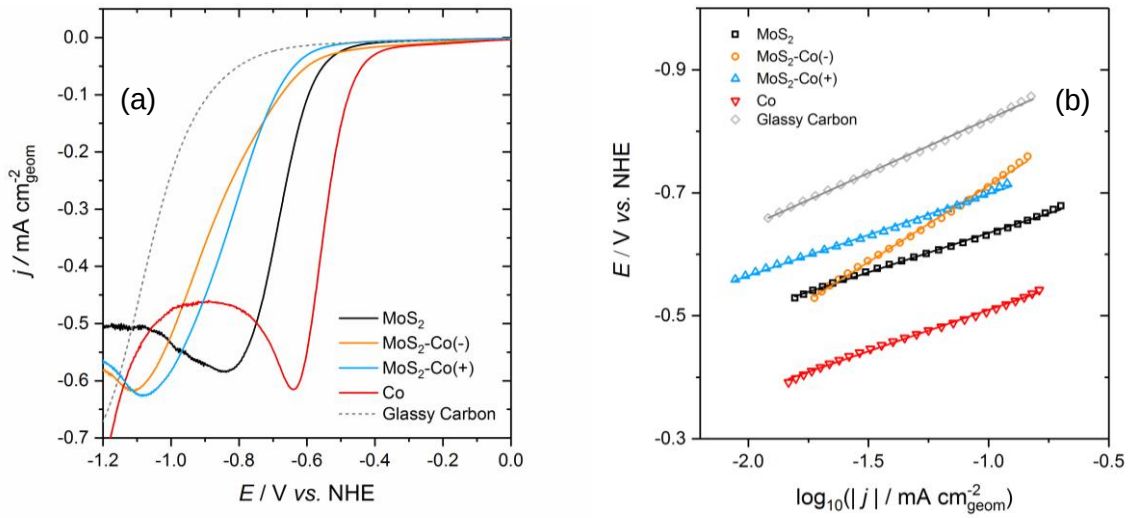

Figure 4. (a) LSVs of the various cluster catalysts and bare glassy carbon, recorded at 25 mV/s in a solution of 0.1 M $NaClO_4$ + 2 mM $HClO_4$ (pH 2.8). (b) Tafel plots for the cluster catalysts, obtained from LSV data recorded at a scan rate of 2 mV/s. For clarity, only every 15th data point is plotted, with the solid lines on the scatter plots indicating the linear region used to calculate the Tafel slope.

The most positive potential for the onset of HER is observed for the pure Co clusters, which reaches a peak current density at -0.64 V. This is followed by pure MoS_2, which peaks at a more negative potential of -0.84 V. Meanwhile, the two Co-doped MoS_2 samples demonstrate a poorer performance than either of the pure cluster materials, with peak potentials of -1.09 V and -1.11 V for MoS_2-Co(+) and MoS_2-Co(-) respectively. The negative shift in the peak potential compared to the pure Co and MoS_2 cluster samples suggests that doping with Co is disadvantageous to electrocatalytic performance. Importantly, the loss of apparent HER activity as a consequence of Co doping is a good indication that the co-deposited Co interacts strongly with the MoS_2 clusters and further confirms that Co does not simply deposit in metallic form on the GC surface.

We note that the onset potentials for the various MoS_2 cluster catalysts fall broadly in the range of –0.4 V to –0.6 V, which are more negative than those typically reported in the literature at pH 0 (*e.g.*

for 2H-MoS_2 nanosheets[1, 2]) even when adjusting for the 165 mV negative Nernstian shift due to the higher pH of 2.8 used in this study. However, the observed onset potentials are comparable to those observed previously for MoS_2 produced by CBD and the slightly poorer apparent performance compared to the wider literature can be attributed to the planar nature of the support and the associated low cluster catalyst loadings.[11] This observation also suggests that the clusters have a low edge site content such that the HER performance is dominated by the intrinsically less active basal plane.

Equivalent LSV measurements were also performed in 0.5 M H_2SO_4 (Figure S3, Supporting Information), wherein the Co clusters significantly outperformed the doped and undoped MoS_2 clusters, reaching a current density of -10 mA cm^{-2}_{geom} at a potential of -0.31 V. Meanwhile, the HER onset behaviour of the various MoS_2 clusters is similar, with MoS_2 and MoS_2-Co(-) showing slightly enhanced catalytic activity compared to MoS_2-Co(+). However, at more negative potentials (-0.8 V) the undoped MoS_2 is found to exhibit notably higher HER current densities than the MoS_2-Co(-) and MoS_2-Co(+) samples, consistent with Co doping resulting in a loss in performance. Whilst we cannot neglect the possibility of Co dissolution in the more strongly acidic (pH 0) environment, these observations indicate that the broad trend observed above is reproducible under conditions more relevant to electrolysis in a proton exchange membrane (PEM) device. Further discussion of this data can be found in the Supporting Information.

Figure 4b illustrates Tafel plots which were calculated using LSV data recorded at 2 mV/s (the data was recorded at a slower scan rate than in Figure 4a to obtain a more accurate estimation of the Tafel slope). The pure MoS_2, pure Co and MoS_2-Co(+) cluster catalysts exhibit similar Tafel slopes, ranging between approximately 120 mV/dec – 130 mV/dec. These values support the occurrence of a Volmer mechanism, in which the adsorption of monatomic hydrogen is the rate determining step, and are consistent with values obtained both for semiconducting 2H-MoS_2,[38] as well as Ni-doped MoS_2 clusters.[11] A previous report on carbon-supported Co nanoparticles indicated that Tafel slopes can range between 96 mV/dec – 156 mV/dec in 0.5 M H_2SO_4,[39] and therefore the slope of 130 mV/dec for the Co clusters is reasonable. The MoS_2-Co(-) sample, which was the poorest performing catalyst based on the LSV data, exhibits an unusually high Tafel slope of 230 mV/dec. The reasons for this are unclear, but close inspection of the corresponding LSV data in Figure 4(a) reveals an unusual shape, making it difficult to isolate a linear Tafel region. Such non-linearity suggests there may be a change of rate determining step as a function of potential which would point towards a more complex HER mechanism on this sample. This mechanistic complexity may be related to the uncertainty in cluster size for the MoS_2-Co(-) sample, compared to the other samples.

Table 1. Summary of total surface area (SA) and HER performance metrics for undoped/doped MoS_2 clusters, pure Co clusters and bare GC substrate.

Sample	**SA / cm^2**	***b* / mV/dec**	**E_{peak} / V**	**$j_{-0.67\ V}$ / mA cm$^{-2}_{geom}$**	**TOF per SA (at -0.67 V) / H_2 s^{-1} cm$^{-2}_{SA}$**
MoS_2	0.026	122	-0.84	-0.28	6.7×10^{15}
MoS_2-Co(-)	0.044	230	-1.11	-0.09	1.2×10^{15}
MoS_2-Co(+)	0.080	131	-1.09	-0.07	5.4×10^{14}
Co	0.100	130	-0.64	-0.59	3.6×10^{15}
Glassy Carbon	0.196	175	-	-0.02	6.2×10^{13}

Table 1 presents a summary of key HER performance metrics for the various samples, including the Tafel slope (*b*), and peak potential (E_{peak}). In addition, the current density recorded at each of the catalysts at a potential of -0.67 V ($j_{-0.67\ V}$), corresponding to the half-wave potential of the pure MoS_2 clusters, is provided as a means to compare the HER performance. This was considered a more meaningful current comparison than estimating an exchange current density by extrapolating the Tafel data to E = 0 V, which is vastly removed from the active potential region of these catalysts. The $j_{-0.67\ V}$ values reflect the trend observed in the voltammetry, indicating that doping MoS_2 with Co leads to the current density falling to approximately a third of that of the undoped material. We note that in the case of Co the reported $j_{-0.67\ V}$ value actually represents a minimum current density, since at -0.67 V the Co cluster response is already in the diffusion-limited regime, but this does not impact the comparison between the MoS_2 samples.

In interpreting the above observations, it is important to consider the effect of the total number of HER active sites present on each sample as this will naturally govern the HER current measured under kinetically-limited conditions. In previous studies, attempts have been made to estimate the number of active sites on MoS_2 samples using electrooxidation.[2, 11] However, in our case such an approach was considered untrustworthy because of the heterogeneous nature of the samples, the large number of possible types of active site and the low catalyst loadings, so instead we elected to consider the total cluster surface area in this context. The estimated total surface areas of each of the samples is presented in Table 1 (see also Section 3.1), from which it is evident that the pure Co and Co-doped MoS_2 samples have a higher surface area than pure MoS_2. Therefore the inferior HER performance of the MoS_2-Co(+) and MoS_2-Co(-) compared to pure MoS_2 cannot be explained by a surface area effect. To verify this, the geometric current density data presented Figure 4(a) was re-normalized to cluster surface area and the resulting LSVs are shown in Figure S2. The plots confirm that Co-doping of MoS_2 leads to an increase in the overpotential required for HER and suggest that the highest Co-doping level leads to the worst HER performance. Furthermore, the $j_{-0.67\ V}$ data presented in Table 1 was used to estimate a turnover frequency (TOF) in molecules of H_2 generated per unit surface area, at a potential of -0.67 V, using the approach reported previously.[11] The TOF data, also presented in Table 1, further validates our

assertion that pure MoS_2 intrinsically outperforms both of the Co-doped MoS_2 samples, in kinetic terms by a factor of between 5 and 10 times. We note that the TOF for the pure Co sample is actually lower than that of the pure MoS_2, however this result is influenced by the fact that the Co LSV has reached the diffusional limit at -0.67V, as discussed above, so this should be considered as a minimum TOF. In contrast, the doped and undoped MoS_2 samples are all under kinetic (or mixed kinetic/diffusion) control at -0.67 V, so comparison of their TOF at this potential should give a reasonable reflection of their relative intrinsic HER activity.

These data clearly demonstrate that Co-doping has a detrimental effect on the intrinsic electrocatalytic HER activity of MoS_2 clusters, which presumably occurs either by a reduction in the number of active sites and/or a decrease in the intrinsic activity of the available active sites. Given the considerable differences in cluster morphology for the two Co-doped samples, it is possible that the poor performance has different origins for the MoS_2-Co(-) and MoS_2-Co(+) samples. Nevertheless, the general observation of catalyst deactivation by Co is in contrast to the previous work highlighted above, which demonstrated that Ni-doping of analogously-prepared MoS_2 leads to performance enhancement.[11]

Moreover, this observation is inconsistent with previous DFT calculations which suggest that Co- and Ni-doping of MoS_2 should have comparable effects, particularly in the case of doping the basal plane,[14] for which a HER performance enhancement is expected. However, the model employed previously did not account for the influence of atomic defects (*e.g.* S-vacancies) in the basal plane, which are well-established as being active sites for the HER.[15, 17, 40, 41] Based on previous studies,[11, 18] MoS_2 clusters produced *via* cluster beam deposition are actually sub-stochiometric in S, as indicated by elemental analysis which suggests that x in MoS_x is between 1.6 and 1.8. This sulphur deficiency is likely to result in a significant number of S-vacancies which, combined with the relatively high aspect ratio of the clusters, suggests that vacancies on the basal plane would have a substantial impact on HER activity. Therefore, it is hypothesized that the origin of the apparent difference might be related to the interaction between dopant atoms and defect sites and their combined effect on the hydrogen affinity of nearby surface sites. In order to understand the differences observed between the two metals on the HER activity of MoS_2, DFT calculations were performed in which the formation and diffusion of sulfur vacancies and dopant atoms in both substitutional and adatom configurations in MoS_2 are considered. Whilst in the previous experimental work on Ni doping of MoS_2 clusters the HER activity enhancement was primarily attributed to edge site modification,[11] our recent computational studies have indicated that the basal plane is more sensitive to doping effects.[14] Therefore, in the present work we focus our attention exclusively on dopant—vacancy interactions on the basal plane.

3.3. Density Functional Theory Calculations

The formation energies of various neutral dopant—vacancy configurations were estimated to determine minimum energy structures and consequently to assess whether there is a repulsive or an attractive interaction between Co/Ni dopants and sulfur vacancies on the MoS_2 basal plane. Dopant atoms in both substitutional (sub_k) and adatom (ad_k) positions were considered, where the index k is a measure of the dopant—vacancy separation (see Figure S4 for further clarification). Specifically, dopants and S vacancies separated by k = 0, 1, 2 and ∞ equivalent doping sites were studied, where the limiting cases k = 0 and k = ∞ correspond to dopant—vacancy pairs and isolated defects, respectively. As an illustration, a few of the studied defect configurations are presented in Figure 5, along with the calculated formation energies. Please refer to the Supporting Information for a detailed technical description of the calculation of formation energies.

Doping of the MoS_2 basal plane with either Co or Ni in adatom positions or introducing a sulfur vacancy result in minor structural changes. Primarily, a slight contraction of adjacent S atoms toward the vacancy is observed upon geometry optimization. On the other hand, substitutional doping of Mo-sites with Co or Ni results in symmetry breaking such that the S-coordination of the metal site decreases from 6 to 5. Therefore, doping with Co or Ni leaves one adjacent sulfur atom with a dangling bond (see the sub_1 site in Figure 5a as an example). Turning to the corresponding formation energies (Figure 5b), the observed trend is evident and independent of the considered impurity atom – both adatom and substitutional Co and Ni dopants prefer to form pairs with sulfur vacancies, and thus there appears to be a considerable attraction between the defects. Specifically, the formation of dopant—vacancy pairs is favoured by more than 1.9 eV and 1.0 eV in the case of substitutional and adatom doping, respectively, compared to infinite defect separation. However, the above results do not yet suggest any significant difference between Co and Ni doping from a thermodynamic point of view.

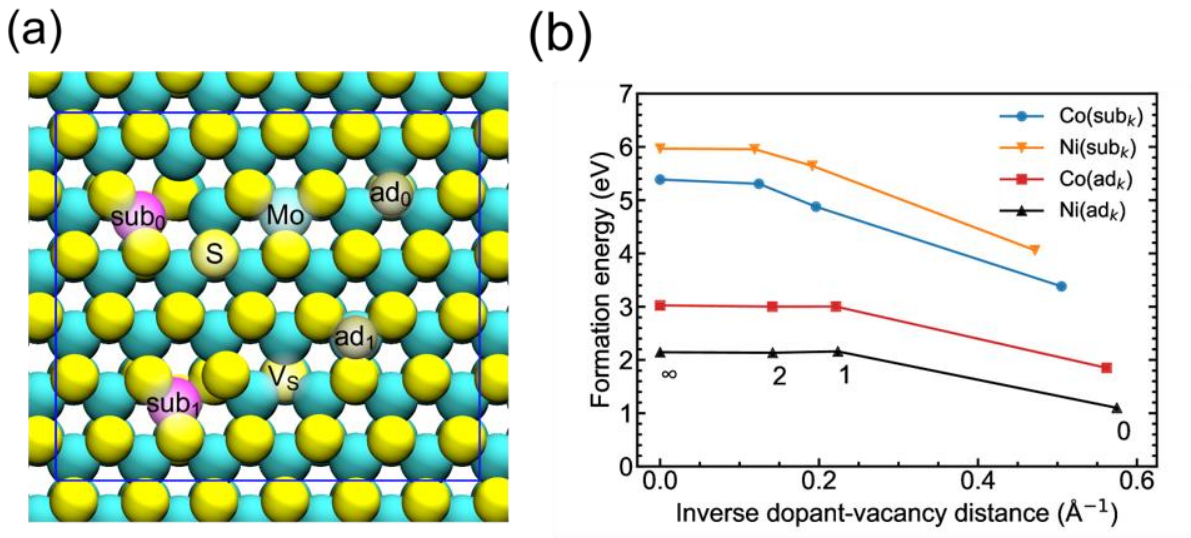

Figure 5. (a) Illustration and definition of studied dopant—vacancy configurations. Yellow, cyan, magenta and brown spheres correspond to S, Mo, Co and Ni atoms, respectively. The "sub_k" and "ad_k" notation refers to dopant atoms in substitutional

and adatom configurations, respectively, with the index *k* denoting the number of equivalent sites between the dopant and the vacancy. Note that this figure serves as an illustrative example and in practice all dopant—vacancy combinations were analysed separately. (b) Total formation energy of a single sulfur vacancy and a Co/Ni dopant in a substitutional or an adatom configuration as a function of the inverse dopant—vacancy distance.

The hydrogen adsorption affinity of various sites around dopant—vacancy configurations was investigated to gain insight into the role of the relative position of dopants and vacancies on the HER activity of the MoS_2 basal plane. Free energies of hydrogen adsorption (ΔG) were estimated by employing the computational hydrogen electrode (CHE) scheme proposed by Nørskov *et al.*,[42, 43] with further details on the model being provided in the Supporting Information. We emphasize that the following treatise relies solely on thermodynamics, and thereby no direct information regarding HER kinetics is obtained. Nevertheless, studying the adsorption energy of the reactive H* intermediate will reveal whether the HER may proceed feasibly from a thermodynamic perspective, *i.e.* with a low overpotential. Furthermore, given that the initial ($H^+ + e^-$) and final (H_2) states are in thermal equilibrium, this treatment will essentially provide a lower limit for the rate-determining activation barriers. In the spirit of the Sabatier principle, the adsorption free energies can be thus used to investigate activity *trends* between different catalyst materials and reaction sites, under the assumption that the reaction mechanism remains unchanged. Ideally, the adsorption free energy should be close to 0 eV to ensure sufficient activation of the adsorbed intermediate as well as to avoid poisoning of the active site. This defines the thermodynamic prerequisite for efficient HER electrocatalysis.[44]

As a reference, we have calculated the adsorption free energy of hydrogen on the pristine MoS_2 basal plane and on the other hand to sites close to Co/Ni dopants and sulfur vacancies. In agreement with our previous studies,[14, 15] hydrogen adsorption to the pristine MoS_2 basal plane is highly endergonic with an adsorption free energy of roughly 1.9 eV. However, introducing a sulfur vacancy or Co/Ni dopants in a substitutional configuration results in a significant activation. Adsorption of hydrogen directly to the S vacancy corresponds to an adsorption free energy of −0.1 eV, while adsorption to the unsaturated S atom adjacent to a substitutional dopant yields a value of −0.3 eV for both Co and Ni. On the other hand, adatom doping and hydrogen adsorption directly on top of the dopant atom yields the adsorption free energies 0.1 eV and 0.6 eV for Co and Ni dopants, respectively. Therefore, evidently, isolated sulfur vacancies and Co/Ni dopants have a considerable activating effect on the MoS_2 basal plane. The activating effect of Co/Ni dopants and S-vacancies is, however, highly local as has been argued in our previous computational studies,[14, 15] where also hydrogen coverage effects have been considered. Improved HER electrocatalysis is therefore proposed to occur only at the defect sites while adjacent sites remain inert ($\Delta G > 1.2$ eV) and disadvantageous for hydrogen adsorption. This suggests that the hydrogen coverages of the considered surfaces are low under operational conditions, justifying the exclusion of hydrogen coverage effects in the present work.

The results for hydrogen adsorption to systems containing both a Co/Ni dopant atom and a sulfur vacancy are presented in the HER free energy diagrams in Figure 6. Additionally, illustrations of each studied adsorption configuration are presented in the Supporting Information (Figure S5). For MoS_2-Co (Figure 6a) with a $k = 1$ separated dopant and vacancy, one can see that hydrogen adsorption to the sulfur vacancy (V_S, sub_1), to the unsaturated S adjacent to the substitutional dopant (S, sub_1) and directly to the Co adatom (Co, ad_1) is favourable with respect to the HER, $|\Delta G| \approx 0.1$ eV. Adsorption to V_S with the dopant in an adatom configuration (ad_1) is on the other hand slightly less preferential, $\Delta G \approx -0.3$ eV. Nevertheless, the obtained adsorption free energies for the Co-doped system with $k = 1$ appear in general to be optimal for the HER. On the other hand, if we consider $k = 0$, *i.e*. dopant—vacancy-pairs, a considerable deactivation of sites is observed. Particularly, the adsorption free energy of hydrogen to the, now saturated, S atom adjacent to the substitutional Co dopant as well as directly to the Co adatom increases by roughly 0.5 eV and 0.9 eV, respectively, which will most certainly result in a lowered HER activity of these sites. Furthermore, the adsorption free energy to the S vacancy with Co in a substitutional position is decreased from −0.1 eV to −0.3 eV, while for Co in the adatom position the S vacancy becomes occupied and is consequently completely eliminated. Considering that the dopant—vacancy pairs correspond to minimum energy structures (Figure 5b), it is concluded that MoS_2 basal planes containing both Co impurities and sulfur vacancies may deactivate over time.

Turning to the MoS_2-Ni system (Figure 6b), a relatively similar behaviour as for MoS_2-Co is observed, *i.e.* minimum energy dopant—vacancy configurations are in general deactivated. However, two important differences arise. First, adsorption directly to the Ni adatom (Ni, ad_1) is considerably endergonic with $\Delta G \approx 0.6$ eV, whereas the Co adatom on MoS_2-Co was found to be rather active. Secondly, and most importantly, adsorption to the S vacancy site in the case of substitutional Ni-doping appears to be less dependent on the dopant—vacancy separation, and in fact a slight *activation* of the site is observed when going from $k = 1$ to the $k = 0$ minimum energy structure with $\Delta G \approx -0.2$ eV → −0.1 eV. The fact that hydrogen adsorption to the V_S site is favourable with respect to the HER for the minimum energy structure is the first evidence that may be used to tentatively explain the reported activity difference between Co- and Ni-doped MoS_2 clusters. Finally, we note that other sites not equivalent to the ones discussed explicitly above, *e.g*. sulfur atoms adjacent to S vacancies or dopant adatoms and other saturated S sites further from dopants/vacancies, exhibit negligible HER activity with corresponding adsorption free energies of more than 1 eV.

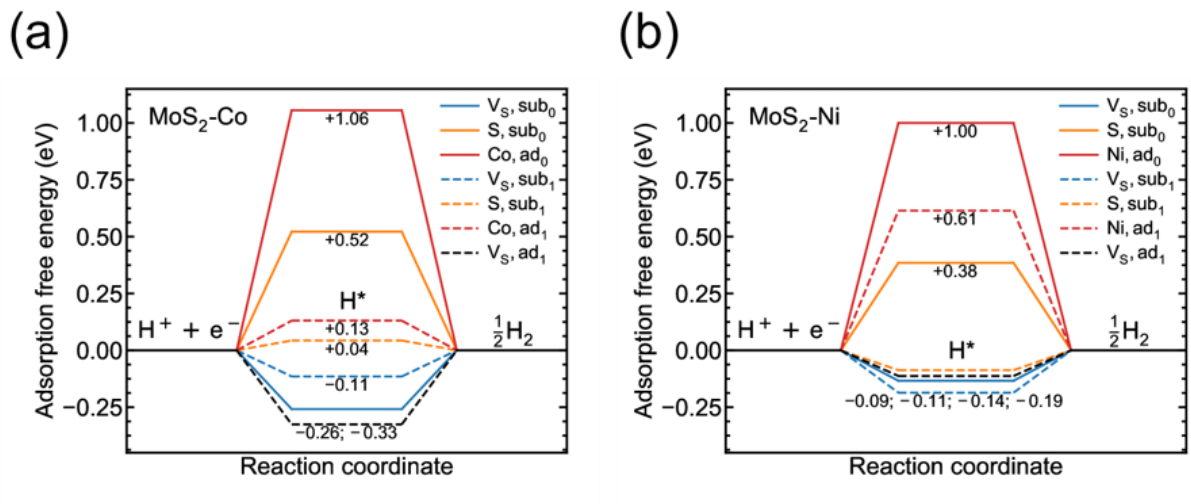

Figure 6. Free energy diagrams for the HER on various sites on the (a) MoS_2-Co and (b) MoS_2-Ni defect basal surfaces. In the legends, the first symbol denotes the hydrogen adsorption site, while the second marks the considered dopant—vacancy configuration. Solid lines correspond to the minimum energy dopant—vacancy configurations, *i.e.* pairs, while dopants and vacancies separated by 1 site are indicated by dashed lines.

However, a key detail left to be assessed is the kinetics of vacancy and dopant adatom diffusion. Indeed, in case that vacancy/adatom diffusion is hindered due to high migration barriers, dopant—vacancy configurations formed during cluster production could be immobilized in which case the importance of the above deactivation processes would be small. To this end, we determine the minimum energy migration paths for S vacancies and dopant adatoms using the climbing image nudged elastic band (CI-NEB) method.[35] Specifically, we have considered for the substitutionally doped systems the diffusion of a sulfur vacancy from the $k = 1$ position to the $k = 0$ position, and for the dopants in adatom positions the migration of the adatom from the $k = 1$ position into the vacancy $k = 0$. As an example, the optimized minimum energy paths for the Co-doped system are presented in Figure 7, along with the obtained relative energy profiles and diffusion rates for all systems.

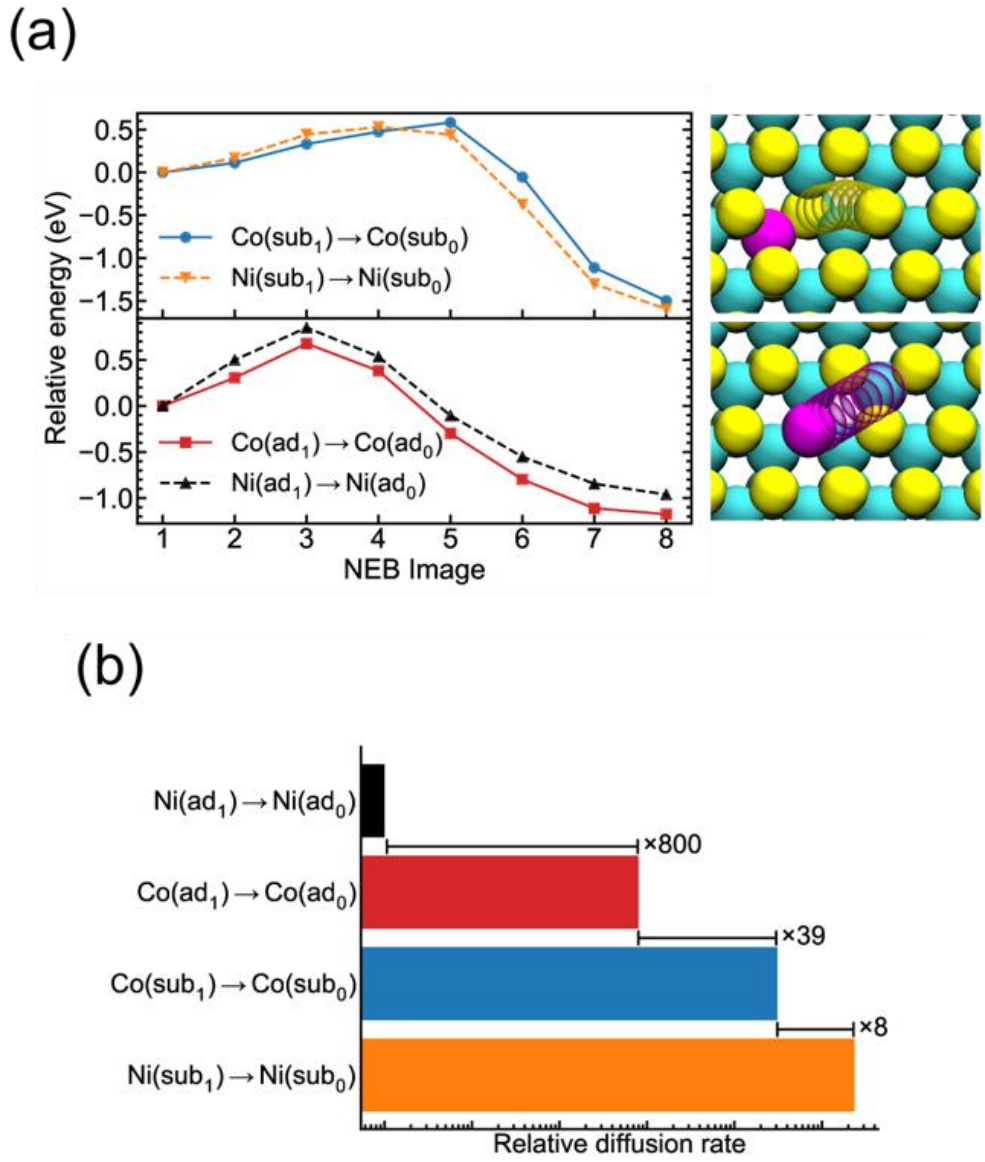

Figure 7. (a) The energy profiles along the minimum energy paths for the considered diffusion/deactivation processes. The optimized migration paths for a sulfur vacancy and a dopant adatom are illustrated to the right, with the Co-doped surface used as an example. Note that only the movement of the migrating atom is illustrated for clarity. In practice, also other nearby atoms were observed to relax slightly along the reaction coordinate. (b) The relative rates of diffusion on the investigated surfaces at T = 300 K.

Again, the calculated energy profiles (Figure 7a) illustrate clearly the preference of S vacancies and Co/Ni dopants to form pairs. The dopant—vacancy combination energy ($k = 1 \rightarrow 0$) is approximately −1.5 eV for the substitutionally doped systems and −1.0 eV for the adatoms. Regarding the activation barriers, the lowest value is observed for the vacancy diffusion on the Ni-doped system ($E^{\ddagger} \approx 0.5$ eV), closely followed by the same process on the MoS_2-Co basal plane $E^{\ddagger} \approx 0.6$ eV. While the diffusion of the Co adatom occurs still with a moderate barrier of 0.7 eV, the activation energy for Ni adatom diffusion is observed to be relatively high, $E^{\ddagger} \approx 0.9$ eV. The relative rates of diffusion in Figure 7b

illustrate the effect of the determined migration barriers on the kinetics of dopant—vacancy combination and have been calculated according to Equation (1),

$$\frac{v}{v_{\text{ref}}} = \exp\left(-\frac{\Delta E^{\ddagger}}{k_{\text{B}}T}\right) \qquad \text{Eq. 1}$$

where v and v_{ref} are the diffusion and reference diffusion rates, respectively; $\Delta E^{\ddagger}$ is the corresponding diffusion activation barrier difference; k_{B} is the Boltzmann constant and T is the absolute temperature. Taking the highest barrier as the reference, we find that the diffusion of the Ni adatom is nearly three orders of magnitude slower than the diffusion of the Co adatom. Moreover, the diffusion of the S vacancy on the Co-doped system is approximately 40 times faster than the migration of the Co adatom, and roughly 10 times slower than the S vacancy diffusion on the Ni-doped system. Considering the above reported deactivation of adsorption sites upon formation of dopant—vacancy pairs, the fact that the Ni adatom diffusion is slow supports well the experimental observations. Indeed, a diffusion barrier of as much as 0.9 eV may be high enough to effectively immobilize Ni adatoms such that the surface remains active with respect to the HER. On the other hand, as the other surfaces exhibit lower barriers and thus faster migration rates, the fact that MoS_2-Co is observed to perform worse than defective MoS_2 without dopants while MoS_2-Ni improves the performance can be understood. Importantly, we note also the slight activation of the S vacancy upon dopant—vacancy combination on the substitutionally doped MoS_2-Ni system. The rate for this process is found to be the fastest, indicative of facile partial activation.

To summarize, our findings from the DFT calculations are threefold: (1) The formation of dopant—vacancy pairs is energetically favoured by more than 1.0 eV in all considered cases, *i.e.* Co and Ni doping in both substitutional and adatom configurations, compared with infinitely separated vacancies and dopants; (2) Formation of dopant—vacancy pairs is in general observed to result in a deactivation of sites around the defect structures, except for the S vacancy site adjacent to a substitutional Ni-dopant which is slightly activated; (3) The dopant—vacancy combination rate is roughly three to five orders of magnitude slower on the MoS_2 basal plane doped with Ni-adatoms compared with the other studied configurations, which follow the trend Co(ad) < Co(sub) < Ni(sub) in combination rate. This suggests that a kinetic effect can explain the observed differences in intrinsic HER activity between Co- and Ni-doped MoS_2, namely that Ni adatoms are immobilized in active configurations, leaving defect sites (S vacancies) unoccupied and accessible for HER catalysis. Additionally, the fast vacancy diffusion on the substitutionally-doped MoS_2-Ni surface results in a slight activation of the V_S site, as observed by the increase in adsorption free energy from approximately -0.2 eV to -0.1 eV. This can be used to rationalize the experimental observation[11] that Ni improves HER reactivity whereas Co-doping inhibits

performance. These conclusions are summarised schematically in Figure 8, which on the left depicts the active dopant—vacancy configurations prior to their combination, while on the right shows the differing HER behaviours resulting from dopant—vacancy pairing. We note that in the comparative work on Ni-doped MoS_2 clusters[11] the key mechanism of HER enhancement was considered to be associated with formation of Ni^{2+}, resulting from aerobic oxidation. However, an improvement in performance was also observed on fresh Ni-doped MoS_2 samples, suggesting that the basal plane enhancement mechanism proposed in this work also contributes to the doping effect. Given that Co doping results in a *decrease* in HER activity, this oxidation mechanism is either not operating in our case, or the positive influence is insufficient to compensate for the loss of activity in the basal plane vacancy sites.

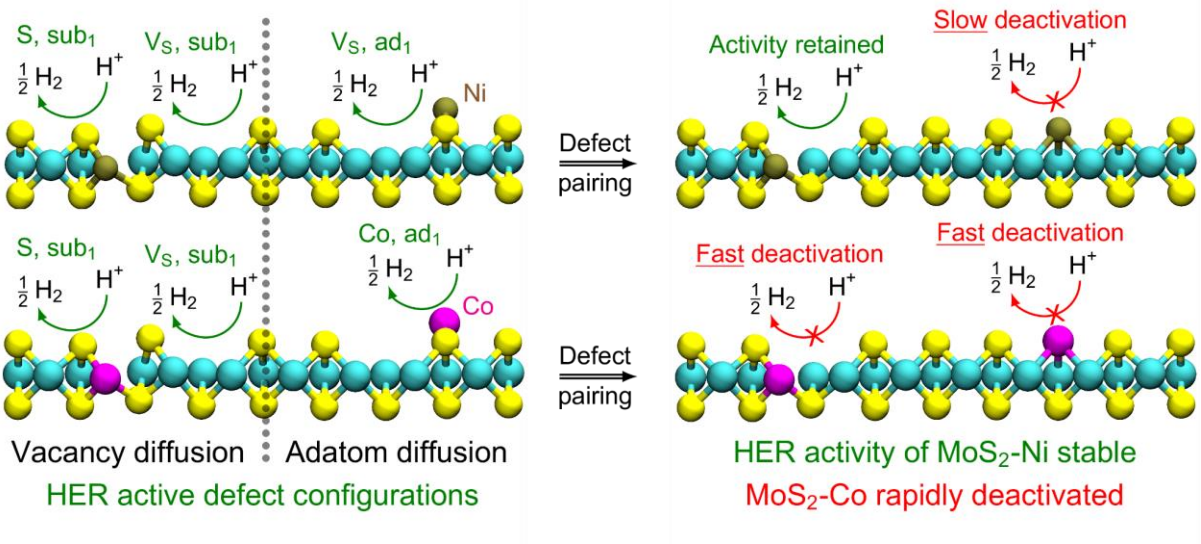

Figure 8. Schematic figure illustrating the differing deactivation behaviours upon dopant-vacancy combination in MoS_2-Ni (top row) and MoS_2-Co (bottom row). S-vacancy diffusion on MoS_2-Ni has no effect on the HER activity of the substitutional dopant—vacancy configuration, while adatom diffusion results in very slow deactivation. In contrast, the corresponding defect pairing processes on MoS_2-Co occur three to four orders of magnitude faster, thus resulting in rapid deactivation. The depicted HER active configurations exhibit ΔG values between -0.2 eV and +0.2 eV based on the results presented in Figures 6a and 6b. The colour coding of atoms is as defined in Figure 5a.

On revisiting the experimental data in light of the above theoretical insights, we note that increasing the Co doping level from very low to very high appears to decrease the measured TOF. At first sight this would appear consistent with the premise that Co deactivates the catalytic sites, as an increase in doping would be expected to measurably worsen the performance unless the active sites are saturated even at the low doping level, which seems unlikely. However, as discussed in Section 3.1, the two levels of Co doping result in considerably different cluster morphologies to the extent that the MoS_2-Co(+) sample,

in which the clusters adopt a core-shell arrangement, ought to be considered as an entirely different material to pure MoS_2 and MoS_2-Co(-). In this sense, it is not possible to confidently assess the effect of doping level, and a more detailed compositional study at low dopant levels would be required to evaluate this phenomenon fully. Nevertheless, whilst the MoS_2-Co(+) clusters differ considerably from the parent material, the morphological similarities between pure MoS_2 and MoS_2-Co(-) enables a valid comparison and supports our assertion that the apparent deactivation is an electronic, rather than structural effect. We note that modelling of individual clusters would potentially reveal insights into size, geometry and morphology effects, but to perform such calculations would be highly challenging considering the number of degrees of freedom involved. Given the complexity of the samples, it is instead much more reasonable to adopt a more fundamental standpoint and consider dopant and vacancy sites in isolation and assume the general observations can be applied irrespective of cluster size.

Finally, it is important to consider our findings in the context of the wider literature, in which there are a number of reports presenting experimental evidence that Co doping is *beneficial* to the HER performance of MoS_2, in contrast with our observations.[2, 10, 45-48] There are several factors relating to sample preparation and catalyst morphology that can account for this apparent conflict. For example, Lau *et al.* showed that Co and Ni doping leads to opposing HER behaviour to our observations, which were attributed to the positive influence of the Co-S interaction compared to the negative influence of the Ni-Mo interaction.[10] However, their work focused on single-layered MoS_2 flakes, rather than multi-layered clusters, which would be expected to have a significant effect on the theoretical and experimental observations. Park and co-workers also observed catalytic enhancement as a result of Co addition but their experimental studies were based on continuous multilayer MoS_2 with Co clusters of a few to ~10 nm deposited on the surface, which differs considerably from our study, which is based on isolated 5 – 10 nm amorphous MoS_2 clusters with sub-nm Co dispersed throughout the particles.[48] Furthermore, their theoretical calculations investigated large (multi-atom) S-vacancies with exposed Mo atoms on monolayer MoS_2, and only explored adatom configurations, which is notably different from the present work, which considers single S-vacancies and includes substitutionally doped configurations. Similarly, improved HER performance upon Co doping of MoS_2 was reported by Dai *et al.* but the rather large average MoS_2 particle size of 70 nm again represents a significant difference compared to our work.[45] Pan and co-workers incorporated Co into the MoS_2 lattice using a solid state synthesis approach, but it is difficult to establish whether the observed HER performance enhancement was predominantly associated with improved electrical conductivity.[46] Finally, Xiong and co-workers reported an enhancement by Co doping but in their case the doping process resulted in a significant (6 fold) increase in electrochemical surface area of the MoS_2 so the intrinsic catalytic performance was not compared.[47] In comparing our results to the literature, it is also important to highlight the fact that our experimental measurements were performed under slightly unconventional HER conditions of

2 mM acid (*i.e.* pH~3 rather than the more commonly employed pH0). Whilst this does not invalidate our conclusions, it is possible that the differing pH could influence the doping trends observed.

The varying reports in the literature as well as the contrasting behaviours against our own observations suggests that the HER performance of TM doped MoS_2 is highly sensitive to the nature of the sample. It is important therefore to highlight that our model is based on the premise that the HER activity of the amorphous MoS_2 clusters produced by CBD is strongly influenced by sulphur monovacancies (as opposed to more extended defect structures) in the basal plane, and that MoS_2 samples produced by different means may deviate from this. For example, in the case of MoS_2 samples exhibiting a low basal plane content (e.g. edge rich materials) or a low concentration of surface monovacancies, the catalytic deactivation phenomena observed in our work may not have a dominant effect on HER performance.

4. Conclusions

Electrochemical HER testing of Co-doped MoS_2 clusters has revealed that, in contrast to the behaviour of Ni-doped MoS_2, the addition of Co has a detrimental effect on the catalytic performance of the clusters. This was indicated by an increase in the overpotential for HER measured in perchlorate electrolyte solution at pH ~3, both for Co-rich and Co-poor hybrid MoS_2 clusters compared with pure MoS_2 material. To unravel the atomistic origin of the experimental results, the interaction between Co and Ni dopants and S-vacancies on the MoS_2 basal plane were studied computationally, offering a rationalization as to the differing behaviour of the two metals. Whereas Co ubiquitously poisons HER-active defects in the basal plane, a phenomenon that is exacerbated by its relatively high dopant mobility, Ni doping can in fact lead to activation of nearby S-vacancies and its relatively low adatom mobility contributes to this advantageous configuration being kinetically stable.

It is important to acknowledge that the real experimental system studied in this work is likely to be substantially more complicated than the system modelled in the DFT study. Indeed, such oversimplification is what led to previous models predicting that TM doping by Co should be beneficial to HER activity and that Ni- and Co-doped MoS_2 should exhibit comparable behaviour. Nevertheless, the results presented have provided new fundamental insights which underline the importance of considering the effect of dopant-vacancy interactions, both from a thermodynamic perspective (binding energy and hydrogen adsorption free energy) and in terms of surface diffusion kinetics, when using doping as a means to improve catalytic activity. This new knowledge could be used to develop a more robust atomistic model for screening TM doping effects in MoS_2 catalysts, which fully incorporates the interplay between dopant atoms and surface defects. Furthermore, our work highlights the potential pitfall of considering the impact of MoS_2 surface morphology and dopant atom in isolation when attempting to experimentally optimise catalytic activity. Finally, the possibility of modifying active

sites in MoS_2 through appropriate choice of metal dopant opens up opportunities for selectively tuning the catalytic behaviour of this material.

Conflicts of Interest

There are no conflicts of interest to declare.

Acknowledgements

This project has received funding from the European Union's Horizon 2020 research and innovation programme under grant agreement No. 686053. The authors gratefully acknowledge Dr. Daniel Escalera-López for helpful discussion.

References

1. T. F. Jaramillo, K. P. Jørgensen, J. Bonde, J. H. Nielsen, S. Horch and I. Chorkendorff, *Science*, 2007, **317**, 100-102.
2. J. Bonde, P. G. Moses, T. F. Jaramillo, J. K. Nørskov and I. Chorkendorff, *Faraday Discuss.*, 2009, **140**, 219-231.
3. J. D. Benck, Z. Chen, L. Y. Kuritzky, A. J. Forman and T. F. Jaramillo, *ACS Catal.*, 2012, **2**, 1916-1923.
4. J. Kibsgaard, Z. Chen, B. N. Reinecke and T. F. Jaramillo, *Nature materials*, 2012, **11**, 963-969.
5. Z. Chen, D. Cummins, B. N. Reinecke, E. Clark, M. K. Sunkara and T. F. Jaramillo, *Nano Lett.*, 2011, **11**, 4168-4175.
6. D. Wang, Z. Pan, Z. Wu, Z. Wang and Z. Liu, *J. Power Sources*, 2014, **264**, 229-234.
7. J. Benson, M. Li, S. Wang, P. Wang and P. Papakonstantinou, *ACS Appl. Mater. Interfaces*, 2015, **7**, 14113-14122.
8. D. Escalera-López, R. Griffin, M. Isaacs, K. Wilson, R. E. Palmer and N. V. Rees, *Applied Materials Today*, 2018, **11**, 70-81.
9. D. Merki, H. Vrubel, L. Rovelli, S. Fierro and X. Hu, *Chem. Sci.*, 2012, **3**, 2515-2525.
10. T. H. M. Lau, X. Lu, J. Kulhavý, S. Wu, L. Lu, T.-S. Wu, R. Kato, J. S. Foord, Y.-L. Soo, K. Suenaga and S. C. E. Tsang, *Chem. Sci.*, 2018, **9**, 4769-4776.
11. D. Escalera-López, Y. Niu, J. Yin, K. Cooke, N. V. Rees and R. E. Palmer, *ACS Catal.*, 2016, **6**, 6008-6017.
12. M. Nielsen, M. E. Björketun, M. H. Hansen and J. Rossmeisl, *Surf. Sci.*, 2015, **631**, 2-7.
13. A. Groß and L. A. Kibler, *Electrocatalysis*, 2017, **8**, 499-500.
14. M. Hakala, R. Kronberg and K. Laasonen, *Sci. Rep.*, 2017, **7**, 15243.
15. R. Kronberg, M. Hakala, N. Holmberg and K. Laasonen, *Phys. Chem. Chem. Phys.*, 2017, **19**, 16231-16241.
16. H. Li, C. Tsai, A. L. Koh, L. Cai, A. W. Contryman, A. H. Fragapane, J. Zhao, H. S. Han, H. C. Manoharan, F. Abild-Pedersen, J. K. Nørskov and X. Zheng, *Nat. Mater.*, 2015, **15**, 48.
17. G. Li, D. Zhang, Q. Qiao, Y. Yu, D. Peterson, A. Zafar, R. Kumar, S. Curtarolo, F. Hunte, S. Shannon, Y. Zhu, W. Yang and L. Cao, *J. Am. Chem. Soc.*, 2016, **138**, 16632-16638.
18. M. J. Cuddy, K. P. Arkill, Z. W. Wang, H.-P. Komsa, A. V. Krasheninnikov and R. E. Palmer, *Nanoscale*, 2014, **6**, 12463-12469.
19. D. Escalera-López, Y. Niu, S. J. Park, M. Isaacs, K. Wilson, R. E. Palmer and N. V. Rees, *Applied Catalysis B: Environmental*, 2018, **235**, 84-91.
20. R. Cai, N. Jian, S. Murphy, K. Bauer and R. E. Palmer, *APL Mater.*, 2017, **5**, 053405.
21. R. E. Palmer, R. Cai and J. Vernieres, *Acc. Chem. Res.*, 2018, **51**, 2296-2304.
22. R. Cai, P. R. Ellis, J. Yin, J. Liu, C. M. Brown, R. Griffin, G. Chang, D. Yang, J. Ren, K. Cooke, P. T. Bishop, W. Theis and R. E. Palmer, *Small*, 2018, **14**, 1703734.
23. J. VandeVondele, M. Krack, F. Mohamed, M. Parrinello, T. Chassaing and J. Hutter, *Comp. Phys. Commun.*, 2005, **167**, 103-128.
24. J. Hutter, M. Iannuzzi, F. Schiffmann and J. VandeVondele, *Wiley Interdiscip. Rev.: Comput. Mol. Sci.*, 2014, **4**, 15-25.
25. G. Lippert, J. Hutter and M. Parrinello, *Mol. Phys.*, 1997, **92**, 477-488.
26. J. P. Perdew, K. Burke and M. Ernzerhof, *Phys. Rev. Lett.*, 1996, **77**, 3865-3868.
27. S. Grimme, J. Antony, S. Ehrlich and H. Krieg, *J. Chem. Phys.*, 2010, **132**, 154104.
28. S. Grimme, S. Ehrlich and L. Goerigk, *J. Comput. Chem.*, 2011, **32**, 1456-1465.
29. E. R. Johnson and A. D. Becke, *J. Chem. Phys.*, 2005, **123**, 024101.
30. J. VandeVondele and J. Hutter, *J. Chem. Phys.*, 2007, **127**, 114105.
31. S. Goedecker, M. Teter and J. Hutter, *Phys. Rev. B*, 1996, **54**, 1703-1710.
32. C. Hartwigsen, S. Goedecker and J. Hutter, *Phys. Rev. B*, 1998, **58**, 3641-3662.
33. M. Krack, *Theor. Chem. Acc.*, 2005, **114**, 145-152.
34. J. VandeVondele and J. Hutter, *J. Chem. Phys.*, 2003, **118**, 4365-4369.
35. G. Henkelman, B. P. Uberuaga and H. Jónsson, *J. Chem. Phys.*, 2000, **113**, 9901-9904.
36. G. J. Martyna and M. E. Tuckerman, *J. Chem. Phys.*, 1999, **110**, 2810-2821.

37. T. Roman and A. Groß, *Catalysis Today*, 2013, **202**, 183-190.
38. C. L. Bentley, M. Kang, F. M. Maddar, F. Li, M. Walker, J. Zhang and P. R. Unwin, *Chem. Sci.*, 2017, **8**, 6583-6593.
39. H. Fei, Y. Yang, Z. Peng, G. Ruan, Q. Zhong, L. Li, E. L. G. Samuel and J. M. Tour, *ACS Appl. Mater. Interfaces*, 2015, **7**, 8083-8087.
40. J. Xie, H. Zhang, S. Li, R. Wang, X. Sun, M. Zhou, J. Zhou, X. W. Lou and Y. Xie, *Adv. Mat.*, 2013, **25**, 5807-5813.
41. L. Madauß, O. Ochedowski, H. Lebius, B. Ban-d'Etat, C. H. Naylor, A. C. Johnson, J. Kotakoski and M. Schleberger, *2D Mat.*, 2016, **4**, 015034.
42. J. K. Nørskov, T. Bligaard, A. Logadottir, J. R. Kitchin, J. G. Chen, S. Pandelov and U. Stimming, *J. Electrochem. Soc.*, 2005, **152**, J23-J26.
43. J. K. Nørskov, J. Rossmeisl, A. Logadottir, L. Lindqvist, J. R. Kitchin, T. Bligaard and H. Jónsson, *J. Phys. Chem. B*, 2004, **108**, 17886-17892.
44. M. T. M. Koper and E. Bouwman, *Angew. Chem. Int.*, 2010, **49**, 3723-3725.
45. X. Dai, K. Du, Z. Li, M. Liu, Y. Ma, H. Sun, X. Zhang and Y. Yang, *ACS Appl. Mater. Interfaces*, 2015, **7**, 27242-27253.
46. J. Pan, C. Song, X. Wang, X. Yuan, Y. Fang, C. Guo, W. Zhao and F. Huang, *Inorganic Chemistry Frontiers*, 2017, **4**, 1895-1899.
47. Q. Xiong, Y. Wang, P.-F. Liu, L.-R. Zheng, G. Wang, H.-G. Yang, P.-K. Wong, H. Zhang and H. Zhao, *Adv. Mat.*, 2018, **30**, 1801450.
48. S. Park, J. Park, H. Abroshan, L. Zhang, J. K. Kim, J. Zhang, J. Guo, S. Siahrostami and X. Zheng, *ACS Energy Letters*, 2018, **3**, 2685-2693.